Reproducible Ohmic bismuth contacts to MoS_2 nanotubes and nanoribbons

Robin T. K. Schock,[1] Stefan Obloh,[1] Korbinian Fink,[1] Matthias Kronseder,[1] Matjaž Malok,[2] Maja Remškar,[2] and Andreas K. Hüttel[1,*]

[1]*Institute for Experimental and Applied Physics, University of Regensburg, 93040 Regensburg, Germany*
[2]*Solid State Physics Department, Institute Jožef Stefan, 1000 Ljubljana, Slovenia*

Attaching metallic contacts to transition metal dichalcogenide nanostructures and in particular to MoS_2 has posed significant challenges over the past years. For MoS_2 nanotubes and nanoribbons, a highly promising material for field effect transistors as well as quantum electronic devices, this is even more the case due to the small, curved surface. So far all attempts there have led to a wide scatter of contact resistances on the same chip. Recently, for quasi two-dimensional, flat MoS_2 flakes, the use of semimetals has led to a breakthrough, making transparent and Ohmic contacts possible. Here, we demonstrate the steps required to reproducibly fabricate contacts to single, vapor phase grown MoS_2 nanotubes and nanowires. All devices display finite room-temperature two-point resistances in absence of gating, with a median value of 340 kΩ in a large fabrication series. A detailed analysis elucidates the impact of the different fabrication changes.

The isolation of few- and monolayer 2d materials such as graphene [1] or transition metal dichalcogenides [2] has led to an avalanche of research regarding both classical semiconductor applications [3–5] and quantum electronics [6–8]. Nevertheless, both commercial chip fabrication where integrated transistor channels become narrower and narrower [9, 10] and quantum electronics with the manyfold focus on one-dimensional physics [11, 12] also point out the intrinsic geometric advantage of quasi-1d nanostructures such as nanotubes, nanoribbons, or nanowires. This has driven recent fundamental research on complex 1d nanomaterials beyond carbon, including even so-called coaxial heterostructures [13].

Molybdenum disulfide MoS_2, mostly known as 2d material and semiconductor [2], also allows the growth of long, straight, low-defect density nanotubes and nanoribbons via chemical vapor deposition [14]. These 1d nanomaterials of large aspect ratio display outstanding optical properties [15, 16] and have shown clear promise in first field effect transistor devices [17]. The central challenge for electronic measurements is however the reliable fabrication of Ohmic contacts. The formation of Schottky barriers at the metal-semiconductor interface [18, 19], often caused or enhanced by Fermi level pinning [19–21], has required significant efforts to overcome [22–24].

For the 2d morphology of MoS_2, i.e., multi- and monolayers, recently breakthrough results have been achieved using semimetal contact layers, in particular bismuth [25, 26] and antimony [27]. A transfer of this technique to 1d morphologies was partially successful [26, 28], with bismuth contacts leading to transparent devices, but at relatively low yield and still a wide scatter of device resistance values.

Here, we demonstrate the reproducible fabrication of MoS_2 nanotube and nanoribbon devices, by combining our experience from previous work [26, 28] with several fabrication techniques developed in other material systems. The results are characterized using room temperature resistance measurements and demonstrate a reduction of the 2-point resistance R_2 scatter by several orders of magnitude, with all measured nanotube and nanoribbon segments displaying $R_2 < 30\,\mathrm{M\Omega}$. Given the extensive interest world-wide in MoS_2 integrated circuits, and the chance provided here to reduce device dimensionality and with it the potential area footprint of transistors, this development is not just interesting for quantum devices but also of clear technological impact as well.

RAW MATERIAL AND DEVICE FABRICATION

Figure 1(a) shows the raw MoS_2 nanomaterial, a mixture of quasi-one dimensional and quasi-two dimensional structures, as deposited on the wall of the growth quartz glass ampoule. The material synthesis via vapor phase deposition is well-established and has been discussed in detail in published literature [14, 28]. Detail optical and scanning electron microscope (SEM) images in Figures 1(b,c) demonstrate the presence of long and crystalline one-dimensional morphologies, including multiwall nanotubes, cf. Fig. 1(d), and nanoribbons, i.e., nanotubes collapsed during growth. The nanomaterial is picked up using a commercially available adhesive tape and deposited on the surface of a p++ Si / SiO_2 wafer with prefabricated grid markers [1, 26, 28]. Subsequently, the surface is imaged in an optical microscope and the location of nanotubes and nanowires is recorded for contact electrode design. As contact material, in either case a bilayer bismuth and gold is deposited, as based on and described in previous work [25, 26, 28]. An additional adhesion layer is not required, since thermally evaporated bismuth bonds sufficiently to a silicon oxide or hBN surface. The drawing of Fig. 1(e) demonstrates an example of a resulting chip geometry, with bond pads, leads, and nanotube regions. The active device region between contacts is chosen to be between 100 nm to 500 nm.

As already discussed previously [26, 28], while highly succesful and reproducible for 2d materials [25], this technique leads for nanotubes and nanoribbons to a few good devices but overall a very large scatter of two-point resistances, with overall insufficient device yield. Consequently, a number of device fabrication optimizations have been developed and tested in combination, listed in the following and discussed in detail further below:

* mail@akhuettel.de

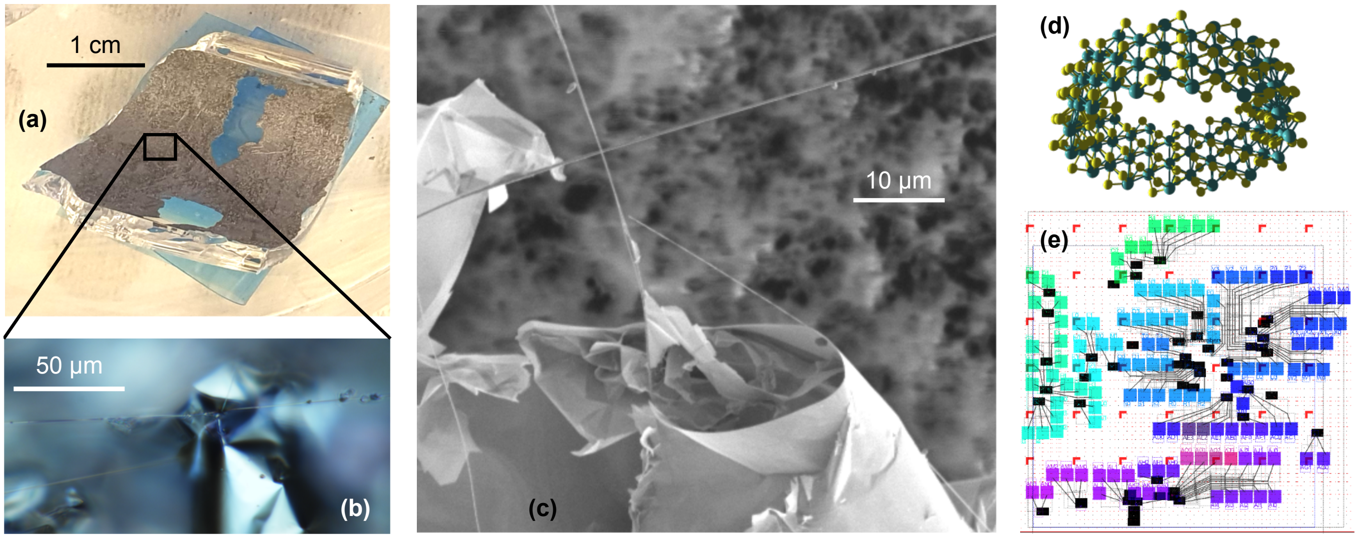

FIG. 1. **Raw material and device geometry.** **a,** As-grown MoS_2 nanomaterial deposited on the wall of a broken growth quartz glass ampoule. **b,** Optical microscope image of the MoS_2 material, with a one-dimensional nanostructure (nanotube or nanoribbon) surrounded by two-dimensional flakes. **c,** Example scanning electron microscope (SEM) image of the MoS_2 nanomaterial, with multiple one-dimensional structures. **d,** Structure model of a short single-wall MoS_2 nanotube segment with chirality (14,14). **e,** Example chip lithography drawing, with contact electrodes (gray lines) and bond pads (colored squares) designed on top of a nanotube/nanoribbon location as detected by optical microscopy (images in black) and position markers (light red background pattern).

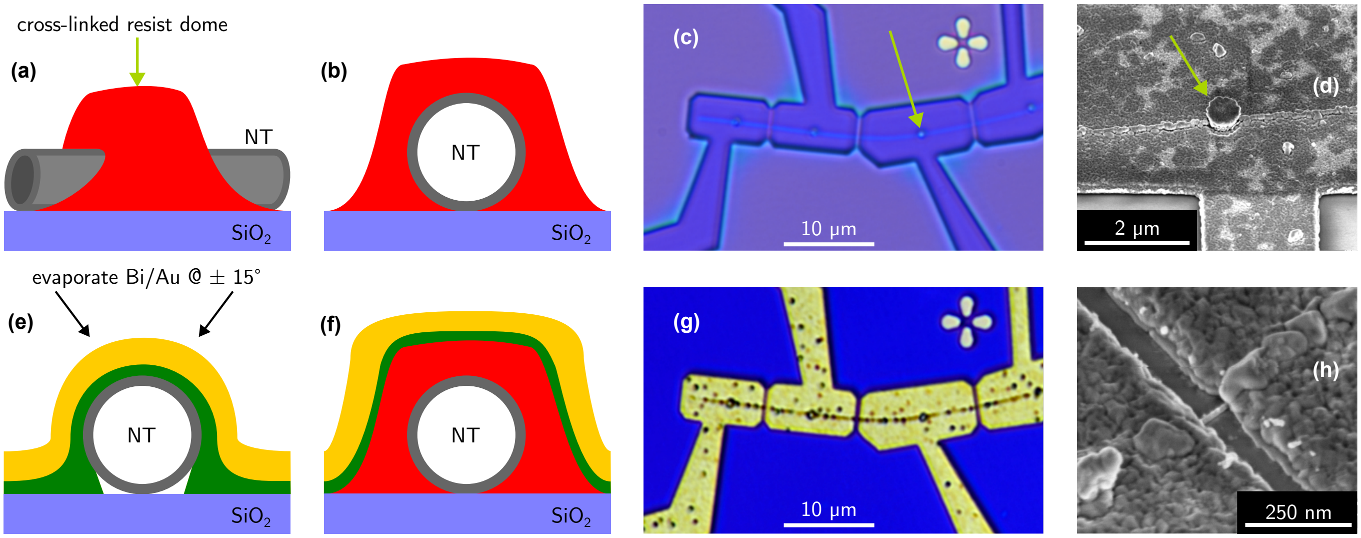

FIG. 2. **Fabrication details.** **a, b,** Sketches illustrating the local crosslinking of PMMA resist to both attach a nanotube to the surface and provide a smooth surface for contact material evaporation. **c,** Optical microscope image of a MoS_2 nanotube device during fabrication, with one of the cross-linked resist domes indicated by a green arrow. **d,** SEM image of a resist dome after evaporation of Bi/Au contacts. **e, f,** Sketches illustrating the improved coverage of a nanotube by dual-angle contact material evaporation, on the blank nanotube as well as in the region of the cross-linked resist dome. **g,** Optical microscope image of the same device as in **c**, now after contact material deposition and lift-off. **h,** SEM image of an active device region, i.e., the measured nanotube segment between contact electrodes.

- **"spot anchoring":** in a small region of the nanotube contact area, poly-methyl metacrylate (PMMA) electron beam lithography resist is strongly overexposed, cross-linking the resist on top of and around the nanotube and creating an effective glue droplet for mechanical stability and possibly a smooth surface topology, see Fig. 1(a–d)
- **deposition pressure:** the ultra-high vacuum setup used for the bismuth and gold deposition is pumped out overnight before each deposition, with the substrate heated to 100 °C, to remove adsorbates and atmospheric contaminants; to further improve the chamber pressure of the evaporation system, titanium is evaporated with

a shutter in front of the device, resulting in a final pressure of $p \simeq 5 \times 10^{-8}$ mbar instead of approximately 3×10^{-7} mbar without these steps;

- **substrate heating:** during the contact deposition process, the heating of the chip substrate with the MoS_2 nanotube to 100 °C is kept up, potentially enabling recrystallization of the bismuth interface layer as discussed below; and finally
- **tilted-angle deposition:** both materials bismuth and gold are evaporated subsequently at two different angles each, i.e. with the substrate rotated by ±15° from the orthogonal incident setting.

Subsequently a lift-off process in hot acetone is performed.

RESULTS

The two-point resistance characterization at room temperature of the tested devices is shown in Fig. 3(a), comparing the straightforward contact deposition by evaporation with the procedure optimized using all the steps as detailed above. A clear reduction in the scatter of resistance values is observed, in conjunction with a decrease in median value. All devices tested here with optimized fabrication display an unabiguous source-drain current upon application of a bias voltage, with resistances below 30 MΩ and a median value of 340 kΩ.

Since previous work has focused also on the effect of the substrate on the device properties [28], Figs. 3(b) and 3(c) display a corresponding sorting of the data points. Fig. 3(b) focuses on the case of a bare, amorphous, and thermally grown silicon oxide, while Fig. 3(c) focuses on devices where the nanotube has been transferred onto a hexagonal boron nitride (hBN) flake [28]. While SiO_2 based devices display slightly lower resistances, same as in [28], the effect of the optimized contact fabrication is clearly visible in both cases, with significantly smaller resistance scatter and a lower median value.

The data of Figure 3(d) is part of a separate, subsequent series of measurements designed to identify the impact of single optimization steps on the device properties. Each column corresponds to a single chip with several nanotubes and nanoribbons, fabricated with one of the optimizations omitted. While the results have to be treated carefully due to fabrication irregularities, this still enables us to draw some conclusions.

Omitting the substrate heating during contact deposition has a clear detrimental effect, indicating that this is indeed a crucial detail. The same to a slightly lesser degree is true of omitting the dual-angle evaporation. A bad vacuum during contact deposition apparently still led to very low-resistive devices, see the middle column in Fig. 3(d); unfortunately, large offsets in the data indicate ground loops that were unnoticed at the time of measurement. This makes a quantitative analysis here unreliable and more measurements would be required for a definite statement; still, the overall trend indicates low two-terminal resistances.

Figure 4 displays typical further characterization results of the chips α, β, and γ of the second measurement series. All devices on the chips were tested for Ohmic behaviour via recording the bias dependence of the current $I(V_{sd})$ at $V_g = 0$. Predominantly, linear behaviour was observed, see, e.g., the measurement of several nanotube segments on chip γ in Fig. 4(a). The only occurences of clear diode-like response were on chip α, where the substrate was not heated during contact deposition. This is demonstrated in Fig. 4(b) with the response of two neighboring segments; the curves nearly coincide when mirroring, indicating that the central, shared contact limits the current here.

Fig. 4(c-e) shows the gate voltage response $I(V_g)$ of devices on the three chips at fixed $V_{sd} = 20$ mV. While in the recorded range $-20\,\mathrm{V} \le V_g \le 20\,\mathrm{V}$ a gate voltage dependence consistent with electron conduction is visible througout, the response is by far strongest for chip γ where no dual-angle evaporation was used.

DISCUSSION

"Spot anchoring"

To ensure that the nanotubes adhere to the substrate surface, as well as to avoid the formation of gaps in the contact material, poly-methyl methacrylate (PMMA) electron beam resist is spun onto the chip and locally over-exposed by a factor ~ 200. This leads to cross-linking of the PMMA molecules, effectively turning the positive resist locally into a highly stable negative-resist and polymer deposition [29], see Fig. 2(b). Fig. 2(c) shows an optical microscope image of a device with the corresponding droplets (green arrow), Fig. 2(d) is a SEM micrograph of a corresponding contact after metal deposition.

The cross-linked PMMA droplets glue the MoS_2 nanomaterial to the chip surface, significantly improving mechanical stability of the devices. This resolves the challenge detailed in [28] (cf. Fig. 8 there), where the MoS_2 nanostructure frequently tears off the chip during lift-off, taking part of the contact metal with it. Furthermore, the polymer deposition can assist a smooth surface transition between the chip substrate and the curved nanotube surface, see the sketch of Fig. 2(b), avoiding shadowing effects and gap formation during contact material deposition and leading to an unbroken contact film. The precise shape of the result depends critically on the resist and contact deposition parameters; as visible in Fig. 2(d), thicker PMMA leads to mushroom-shaped polymer structures.

Chips α, β, γ of the second test series each contained devices with and without PMMA droplets. Electronic characterization showed no clear difference among devices with finite current. This confirms that the main impact of the PMMA droplets is to provide mechanical stability and keep the nanotube or nanoribbon in place.

Deposition pressure

The contact material deposition is performed in an UHV chamber system via electron beam assisted evaporation. In order to reduce contamination with adsorbates and improve

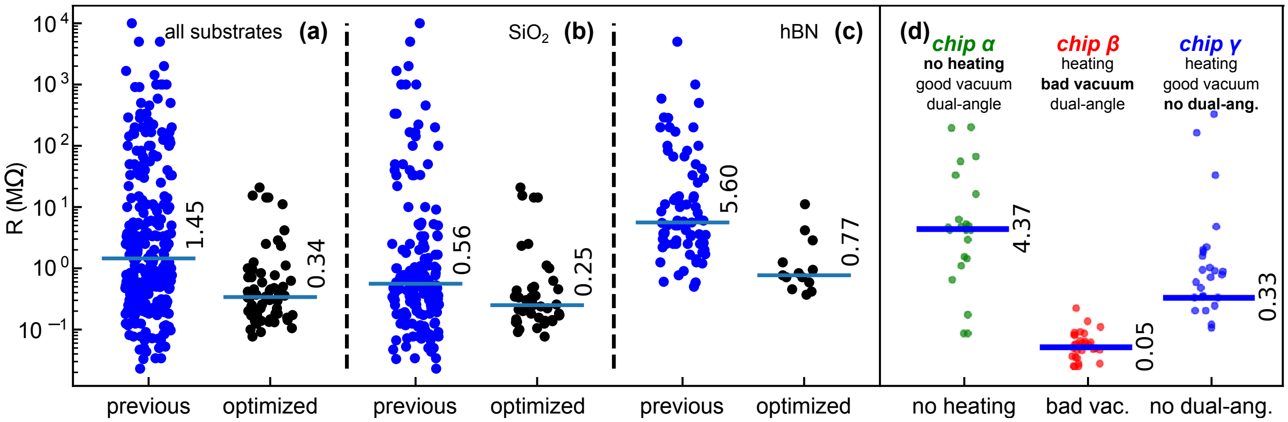

FIG. 3. **Device resistance distribution** **a,** left, blue: distribution of two-point resistances for non-optimized fabrication, showing a wide scatter, data partially already shown in [28]; right, black: optimized fabrication result using all described steps; the scatter of resistance values is reduced by several orders of magnitude. In each case the median value is written out and indicated by a horizontal line. **b,** analogue plots of the subset of measurements where a SiO_2 substrate was directly used; **c,** subset of measurements where the nanotube was deposited onto a hBN flake. The scatter is reduced similarly in both cases. **d,** Separate fabrication data set, where in each column one optimization step was omitted to obtain insights into the underlying mechanisms; chip α: no substrate heating, chip β: bad deposition vacuum (but also see text), chip γ: no dual-angle evaporation.

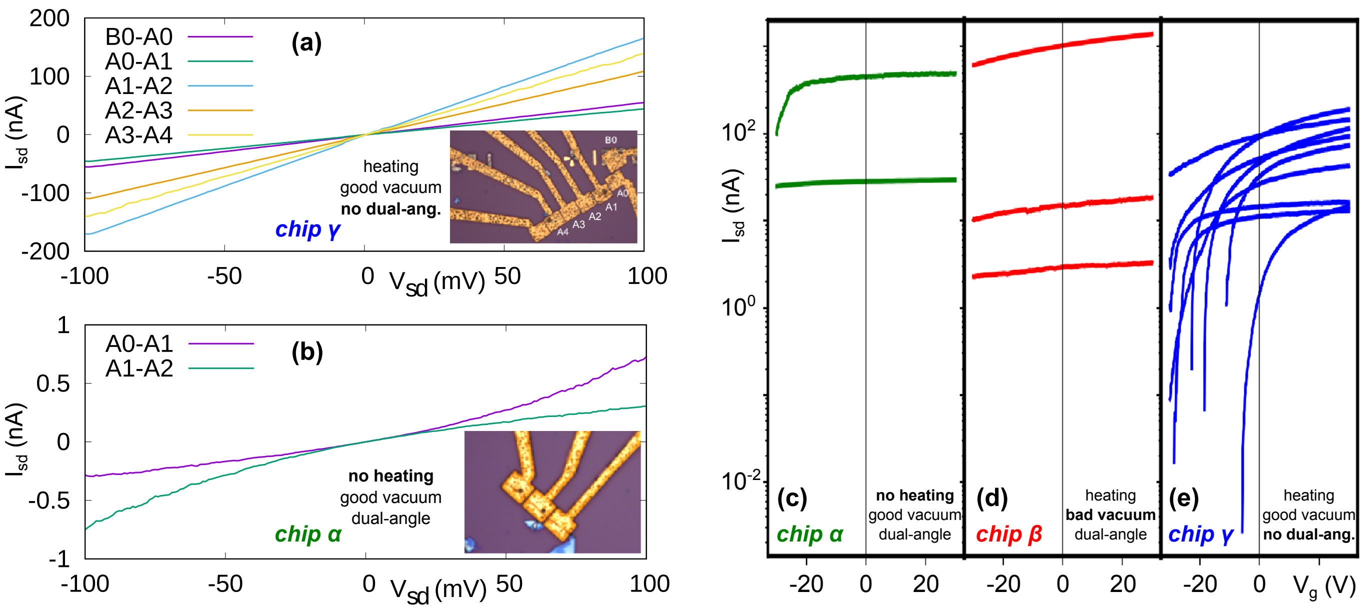

FIG. 4. **Typical device characteristics** **a,** Bias voltage dependence of the current $I(V_{sd})$ at $V_g = 0$ for several nanotube segments on chip γ (cf. Fig. 3(d)). Ohmic behaviour is observed. Inset: optical microscope image of the measured device. **b,** Example bias voltage dependence of the current $I(V_{sd})$ at $V_g = 0$ for two nanotube segments on chip α, with clear diode behavior. Inset: optical microscope image of the measured device. **c,d,e,** Gate voltage dependence of the device current $I(V_g)$ at $V_{sd} = 20\,\text{mV}$ for selected devices on chips α, β, γ.

the interface quality, the devices are heated to 100°C inside the UHV system for > 10 h before deposition. Additionally, a short Ti gettering step is performed to further reduce the pressure of the evaporation system to $p = 5 \times 10^{-8}$ mbar.

Similar optimization steps were performed in early high-profile works on carbon nanotubes that used comparable fabrication [30–32]. Adsorbates or chemical surface modifications can have a strong impact on the interface properties of low-dimensional materials and the Schottky barrier [19], as also attested by a large body of complex and sometimes contradicting published experimental results on 2d MoS_2 devices. Recent studies have revealed that the quality of Ni contacts to MoS_2 depends heavily on the vacuum, with typically ~ 3 times lower contact resistance going from HV to UHV deposition conditions [33].

The authors of Ref. [33] could not identify any significant improvement in contact resistance for Bi contacts for different vacuum conditions. This is consistent with our observations when skipping the vacuum optimization alone (chip β), where this step turns out not to be critical on a smaller test scale, but even led to surprisingly good contacts. Further test would be required to confirm or refute whether a good vacuum has advantages.

Contact materials

The choice of a bismuth / gold bilayer as contact material for MoS_2 was first championed in [25] for flake-based 2d material devices, with outstanding results. Many earlier attempts at Ohmic contacts to MoS_2 had been unsuccessful due to Fermi level pinning and Schottky barrier formation. Low work function metals such as titanium or scandium are a possible solution [34, 35], however tend to react with the MoS_2 surface on deposition [36], particularly detrimental in the low-dimensional material case and for low-temperature applications. Doping with copper [37] or yttrium [38] has in general shown good results, but does not make much sense for nanotubes due to the small surface area involved and the resulting electrostatic potential irregularities.

Instead, bismuth as semimetal was chosen since its vanishing density of states at the Fermi edge avoids the formation of metal-induced gap states and with it Fermi level pinning [20, 21, 25]. Calculations indicate that the effective contact resistance results from an interplay of the absence of interaction (leading to an absence of metal-induced gap states) and the absence of tunneling (leading to a suppression of current), close to the optimum for adjacent 2d layers [39]. For nanotubes, the curvature of the surface as well as the resulting more complex contact material deposition and morphology can then easily explain the remaining resistance fluctuations.

While antimony delivers even better results for 2d material devices [27], specifically for nanotubes and nanoribbons measurements have demonstrated bismuth to be the best choice [28]. A detailed explanation for this is still missing; one can speculate that a bismuth layer may be less sensitive to the curved nanotube surface or the precise deposition conditions, see also the discussion on recrystallization below.

Deposition protocol

The contact materials, bismuth and gold, are deposited with 50 nm and 100 nm at rates of $0.03\,\mathrm{nm\,s^{-1}}$ and $0.05\,\mathrm{nm\,s^{-1}}$, respectively. The substrate is kept heated at 100 °C and the incidence angle of the deposition is changed from $-15°$ to $15°$ after half the layer thickness has been reached for each material to improve coverage. After deposition, the device is left inside the UHV chamber until reaching ambient temperature.

Thermal evaporation, while providing high quality thin films, is a directed process. As a consequence, shadowing and capping effects can occur when surface features such as the nanotubes here are of similar or larger scale as the film thickness [28], an effect that is in literature also deliberately used for device structuring [40]. Dual angle evaporation reduces this, with the material reaching into gaps and below overhangs. Its specific advantage is confirmed by the measurement of chip γ, where without dual angle evaporation clearly increased resistance scatter and median value is observed, see Fig. 3(d). Additionally, without dual-angle evaporation, a stronger gate effect is visible, see Fig. 4(e). As unfortunate side effect, better coverage of the nanotube or nanoribbon appears to lead to partial shielding of the gate voltage.

Bismuth has comparatively low melting point of $T = 271°\mathrm{C}$. It tends to form crystallites during thin film deposition [41]; this is visible in, e.g., Fig. 2(d,h) both for the contact surface away from the nanotube and for additional nucleation directly on top of it, even with the additional gold capping layer. Early research has already addressed the dependence of the crystal formation on the substrate temperature [41, 42], indicating that higher temperature leads to better film quality. This is consistent with the observation that chip α of the second test series, where substrate heating was omitted, was the only one to display Schottky diode behaviour, see Fig. 4(b). Furthermore, for our bismuth / gold bilayer, it is likely that heating effects during the subsequent gold deposition lead to (partial) melting and recrystallization, improving contact transparency [43]. The formation of the gold/bismuth intermetallic compound maldonite (Au_2Bi) at the interface [44] is also possible and has likely been observed by us in a single device where the contacts surprisingly displayed superconductivity phenomena at cryogenic temperature [45], but seems to be the exception.

Substrate

A surprising observation, here as already in [28], is the statistically clearly higher device resistance in case of a hexagonal boron nitride (hBN) substrate. While the amorphous SiO_2 is known for its dangling bonds and surface charges, hBN has been the material of choice to precisely avoid such effects. As a possible cause, the more complex fabrication of hBN-based devices stands out: here, the hBN flakes have to be exfoliated and deposited onto the chip substrate, and subsequently also the MoS_2 nanomaterial has to be transferred again [28]. Each such step increases the risk of surface contamination and structural damage.

CONCLUSIONS AND OUTLOOK

We have managed to improve the fabrication of metallic contacts to MoS_2 nanotubes and nanoribbons such that we consistently achieve Ohmic contacts, with a median 2-point resistance of a segment of 340 kΩ in a large fabrication series. The impact of separate improvements is tested and discussed. Decisive steps include local PMMA crosslinking for mechanical stabilization, substrate heating to 100°C during contact deposition, and dual-angle evaporation to improve coverage of the non-planar nanomaterial. The precise impact of deposition pressure is so far unclear.

In previous work, the integration of MoS_2 nanotubes and nanoribbons into complex devices was challenging due to low fabrication yield. With reliable contact formation, the path towards 1d MoS_2 transistors as well as 1d MoS_2 quantum electronics is now open.

What has not been adressed here is the intrinsic surface quality of the MoS_2 nanotubes and nanoribbons as well as the impact of their geometry. Sulfur vacancies have been reported to be beneficial for n-type contacts [46], but also modify the nanomaterial properties in between them; fabrication in inert environment and treatment with H_2S [47] or thioles [48] may help here. Wall curvature, inner substructures, and deformation on substrate deposition modify the electronic properties [49, 50]. A smaller number of nanotube walls will likely improve reproducibility of device properties; free single-wall MoS_2 nanotubes are thermodynamically unstable [51], but the recent development of coaxial heterostructures provides a path to solve this problem [13].

In the end, while challenges in nanomaterial chemistry and device technology remain, the appeal of truly one-dimensional MoS_2 for both traditional and quantum electronics remains very much undiminished, and a significant step has been made towards device implementation.

ACKNOWLEDGMENTS

The authors gratefully acknowledge funding by the DFG via grants Hu 1808/4-1 (project id 438638106) and Hu 1808/6-1 (project id 438640730) and by the Slovenian Research Agency via grants P1-0099 and PR-11224. M. K. was funded by the DFG via CRC/SFB 1277 (project id 314695032). We would like to thank Lain-Jong Li for insightful discussions and Ch. Strunk, D. Weiss, and F. Kuemmeth for the use of experimental facilities. The measurement data was recorded using Lab::Measurement [52].

AUTHOR CONTRIBUTIONS

The MoS_2 nanomaterial was grown at Jozef Stefan Institute by M. M. The devices were fabricated by R. T. K. S., S. O., and K. F. with help from M. K. The room temperature current measurements were performed by R. T. K. S., S. O., and K. F. The manuscript was written by A. K. H. and R. T. K. S. and reviewed and revised by all coauthors. The project was supervised by M. R. in Ljubljana and by A. K. H. in Regensburg.

COMPETING INTERESTS

The authors declare no competing interests.

DATA AVAILABILITY

The datasets generated during and/or analysed during this study are available from the corresponding author on reasonable request.

[1] Novoselov, K. S. *et al.* Electric field effect in atomically thin carbon films. *Science* **306**, 666–669 (2004). URL https://www.science.org/doi/10.1126/science.1102896.

[2] Novoselov, K. S. *et al.* Two-dimensional atomic crystals. *Proceedings of the National Academy of Sciences* **102**, 10451–10453 (2005). URL https://www.pnas.org/content/102/30/10451.

[3] Das, S. *et al.* Transistors based on two-dimensional materials for future integrated circuits. *Nature Electronics* **4**, 786–799 (2021). URL https://www.nature.com/articles/s41928-021-00670-1.

[4] Dorow, C. J. *et al.* Exploring manufacturability of novel 2D channel materials: 300mm wafer-scale 2D NMOS & PMOS using MoS_2, WS_2, & WSe_2. In *2023 International Electron Devices Meeting (IEDM)*, 1–4 (2023). URL https://dx.doi.org/10.1109/IEDM45741.2023.10413874.

[5] Chou, A.-S. *et al.* Status and performance of integration modules toward scaled CMOS with transition metal dichalcogenide channel. In *2023 International Electron Devices Meeting (IEDM)*, 1–4 (2023). URL https://dx.doi.org/10.1109/IEDM45741.2023.10413779.

[6] Jing, F.-M. *et al.* Gate-controlled quantum dots based on 2D materials. *Advanced Quantum Technologies* **5**, 2100162 (2022). URL https://dx.doi.org/10.1002/qute.202100162.

[7] Liu, X. & Hersam, M. C. 2D materials for quantum information science. *Nature Reviews Materials* **4**, 669–684 (2019). URL https://www.nature.com/articles/s41578-019-0136-x.

[8] Qiu, D. *et al.* Recent advances in 2D superconductors. *Advanced Materials* **33**, 2006124 (2021). URL https://onlinelibrary.wiley.com/doi/abs/10.1002/adma.202006124.

[9] Hills, G. *et al.* Modern microprocessor built from complementary carbon nanotube transistors. *Nature* **572**, 595–602 (2019). URL https://www.nature.com/articles/s41586-019-1493-8.

[10] Si, J. *et al.* A carbon-nanotube-based tensor processing unit. *Nature Electronics* **7**, 684–693 (2024). URL https://www.nature.com/articles/s41928-024-01211-2.

[11] Stern, A. & Lindner, N. H. Topological quantum computation—from basic concepts to first experiments. *Science* **339**, 1179–1184 (2013). URL https://www.science.org/doi/10.1126/science.1231473.

[12] Frolov, S. M. *et al.* Data sharing helps avoid "smoking gun" claims of topological milestones. *Science* **391**, 137–142 (2026). URL https://www.science.org/doi/abs/10.1126/science.adk9181.

[13] Xiang, R. *et al.* One-dimensional van der Waals heterostructures. *Science* **367**, 537–542 (2020). URL https://www.science.org/doi/10.1126/science.aaz2570.

[14] Remskar, M., Skraba, Z., Cléton, F., Sanjinés, R. & Lévy, F. MoS_2 as microtubes. *Appl. Phys. Lett.* **69**, 351–353 (1996).

URL https://dx.doi.org/10.1063/1.118057.
[15] Kazanov, D. R. *et al.* Multiwall MoS_2 tubes as optical resonators. *Applied Physics Letters* **113**, 101106 (2018). URL https://dx.doi.org/10.1063/1.5047792.
[16] Remskar, M. *et al.* Confinement related phenomena in MoS_2 tubular structures grown from vapour phase. *Israel Journal of Chemistry* **62**, e202100100 (2022). URL https://dx.doi.org/10.1002/ijch.202100100.
[17] Fathipour, S. *et al.* Synthesized multiwall MoS_2 nanotube and nanoribbon field-effect transistors. *Appl. Phys. Lett.* **106**, 022114 (2015). URL https://dx.doi.org/10.1063/1.4906066.
[18] Schottky, W. Zur Halbleitertheorie der Sperrschicht- und Spitzengleichrichter. *Zeitschrift für Physik* **113**, 367–414 (1939). URL https://dx.doi.org/10.1007/BF01340116.
[19] Tung, R. T. The physics and chemistry of the Schottky barrier height. *Applied Physics Reviews* **1**, 011304 (2014). URL https://aip.scitation.org/doi/10.1063/1.4858400.
[20] Louie, S. G. & Cohen, M. L. Electronic structure of a metal-semiconductor interface. *Physical Review B* **13**, 2461–2469 (1976). URL https://dx.doi.org/10.1103/PhysRevB.13.2461.
[21] Mönch, W. Valence-band offsets and Schottky barrier heights of layered semiconductors explained by interface-induced gap states. *Applied Physics Letters* **72**, 1899–1901 (1998). URL https://dx.doi.org/10.1063/1.121220.
[22] Gong, C., Colombo, L., Wallace, R. M. & Cho, K. The unusual mechanism of partial Fermi level pinning at metal–MoS_2 interfaces. *Nano Letters* **14**, 1714–1720 (2014). URL https://dx.doi.org/10.1021/nl403465v.
[23] Kim, C. *et al.* Fermi level pinning at electrical metal contacts of monolayer molybdenum dichalcogenides. *ACS Nano* **11**, 1588–1596 (2017). URL https://dx.doi.org/10.1021/acsnano.6b07159.
[24] Sotthewes, K. *et al.* Universal Fermi-level pinning in transition-metal dichalcogenides. *The Journal of Physical Chemistry C* **123**, 5411–5420 (2019). URL https://dx.doi.org/10.1021/acs.jpcc.8b10971.
[25] Shen, P.-C. *et al.* Ultralow contact resistance between semimetal and monolayer semiconductors. *Nature* **593**, 211–217 (2021). URL https://dx.doi.org/10.1038/s41586-021-03472-9.
[26] Schock, R. T. K. *et al.* Non-destructive low-temperature contacts to MoS_2 nanoribbon and nanotube quantum dots. *Advanced Materials* **35**, 2209333 (2023). URL https://dx.doi.org/10.1002/adma.202209333.
[27] Li, W. *et al.* Approaching the quantum limit in two-dimensional semiconductor contacts. *Nature* **613**, 274–279 (2023). URL https://dx.doi.org/10.1038/s41586-022-05431-4.
[28] Schock, R. T. K. *et al.* Material transfer and contact optimization in MoS_2 nanotube devices. *physica status solidi (b)* **262**, 2400366 (2025). URL https://onlinelibrary.wiley.com/doi/abs/10.1002/pssb.202400366.
[29] Zailer, I., Frost, J. E. F., Chabasseur-Molyneux, V., Ford, C. J. B. & Pepper, M. Crosslinked PMMA as a high-resolution negative resist for electron beam lithography and applications for physics of low-dimensional structures. *Semiconductor Science and Technology* **11**, 1235 (1996). URL https://dx.doi.org/10.1088/0268-1242/11/8/021.
[30] Jarillo-Herrero, P., Sapmaz, S., Dekker, C., Kouwenhoven, L. P. & van der Zant, H. S. J. Electron-hole symmetry in a semiconducting carbon nanotube quantum dot. *Nature* **429**, 389–392 (2004). URL https://www.nature.com/articles/nature02568.
[31] Jarillo-Herrero, P. *et al.* Orbital Kondo effect in carbon nanotubes. *Nature* **434**, 484–488 (2005). URL https://www.nature.com/articles/nature03422.
[32] Jarillo-Herrero, P. (2007). Private communication.
[33] Sun, Z. *et al.* Low contact resistance on monolayer MoS_2 field-effect transistors achieved by CMOS-compatible metal contacts. *ACS Nano* **18**, 22444–22453 (2024). URL https://dx.doi.org/10.1021/acsnano.4c07267.
[34] Das, S., Chen, H.-Y., Penumatcha, A. V. & Appenzeller, J. High performance multilayer MoS_2 transistors with scandium contacts. *Nano Letters* **13**, 100–105 (2013). URL https://dx.doi.org/10.1021/nl303583v.
[35] Reinhardt, S., Pirker, L., Bäuml, C., Remškar, M. & Hüttel, A. K. Coulomb blockade spectroscopy of a MoS_2 nanotube. *physica status solidi (RRL) – Rapid Research Letters* **13**, 1900251 (2019). URL https://dx.doi.org/10.1002/pssr.201900251.
[36] Wu, R. J. *et al.* Visualizing the metal-MoS_2 contacts in two-dimensional field-effect transistors with atomic resolution. *Phys. Rev. Materials* **3**, 111001 (2019). URL https://dx.doi.org/10.1103/PhysRevMaterials.3.111001.
[37] Liu, M. *et al.* Improvement of metal-semiconductor contact from Schottky to Ohmic by Cu doping in transition metal dichalcogenide transistors. In *2018 IEEE 13th Nanotechnology Materials and Devices Conference*, 1–4 (IEEE, Portland, OR, USA, 2018). URL https://ieeexplore.ieee.org/document/8605891/.
[38] Jiang, J. *et al.* Yttrium-doping-induced metallization of molybdenum disulfide for Ohmic contacts in two-dimensional transistors. *Nature Electronics* **7**, 545–556 (2024). URL https://www.nature.com/articles/s41928-024-01176-2.
[39] Lizzit, D., Khakbaz, P., Driussi, F., Pala, M. & Esseni, D. Ohmic behavior in metal contacts to n/p-type transition-metal dichalcogenides: Schottky versus tunneling barrier trade-off. *ACS Applied Nano Materials* (2023). URL https://doi.org/10.1021/acsanm.3c00166.
[40] Chen, Y. *et al.* Gate-tunable superconductivity in hybrid InSb–Pb nanowires. *Applied Physics Letters* **123**, 082601 (2023). URL https://dx.doi.org/10.1063/5.0155663.
[41] Kumari, L. *et al.* Effects of deposition temperature and thickness on the structural properties of thermal evaporated bismuth thin films. *Applied Surface Science* **253**, 5931–5938 (2007). URL https://dx.doi.org/10.1016/j.apsusc.2006.12.125.
[42] Partin, D. L., Thrush, C. M., Heremans, J., Morelli, D. T. & Olk, C. H. Growth and characterization of epitaxial bismuth films. *Journal of Vacuum Science & Technology B: Microelectronics Processing and Phenomena* **7**, 348–353 (1989). URL https://doi.org/10.1116/1.584748.
[43] Li, L.-J. (2024). Private communication.
[44] Okamoto, H. & Massalski, T. B. The Au-Bi (gold-bismuth) system. *Bulletin of Alloy Phase Diagrams* **4**, 401–407 (1983). URL https://dx.doi.org/10.1007/BF02868093.
[45] de Haas, W. J. & Jurriaanse, F. The super-conductivity of gold-bismuth. *Naturwissenschaften* **19**, 706–706 (1931).
[46] McDonnell, S., Addou, R., Buie, C., Wallace, R. M. & Hinkle, C. L. Defect-dominated doping and contact resistance in MoS_2. *ACS Nano* **8**, 2880–2888 (2014). URL https://dx.doi.org/10.1021/nn500044q.
[47] Pető, J. *et al.* Spontaneous doping of the basal plane of MoS_2 single layers through oxygen substitution under ambient conditions. *Nature Chemistry* **10**, 1246–1251 (2018). URL https://www.nature.com/articles/s41557-018-0136-2.
[48] Schwarz, A. *et al.* Thiol-based defect healing of WSe_2 and WS_2. *npj 2D Materials and Applications* **7**, 1–9 (2023). URL https:

//www.nature.com/articles/s41699-023-00421-0.

[49] Malok, M., Jelenc, J., Krajnc, A. P. & Remškar, M. Edge and defect effects on charge distribution in collapsed MoS_2 nanotubes. *Nanoscale Advances* **7**, 8161–8169 (2025). URL https://dx.doi.org/10.1039/D5NA00771B.

[50] Malok, M., Jelenc, J. & Remškar, M. Electrical properties of collapsed MoS_2 nanotubes. *Nanoscale* **17**, 12361–12370 (2025). URL https://dx.doi.org/10.1039/D5NR00284B.

[51] Khadiev, A. *et al.* Misfit layered compounds: Insights into chemical, kinetic, and thermodynamic stability of nanophases. *Accounts of Chemical Research* **57**, 3243–3253 (2024). URL https://pubs.acs.org/doi/10.1021/acs.accounts.4c00412.

[52] Reinhardt, S. *et al.* Lab::Measurement — a portable and extensible framework for controlling lab equipment and conducting measurements. *Computer Physics Communications* **234**, 216 (2019). URL https://dx.doi.org/10.1016/j.cpc.2018.07.024.